Volume 51
Number 41
7 November 2022
Pages 15617-16030

Dalton Transactions

An international journal of inorganic chemistry

rsc.li/dalton

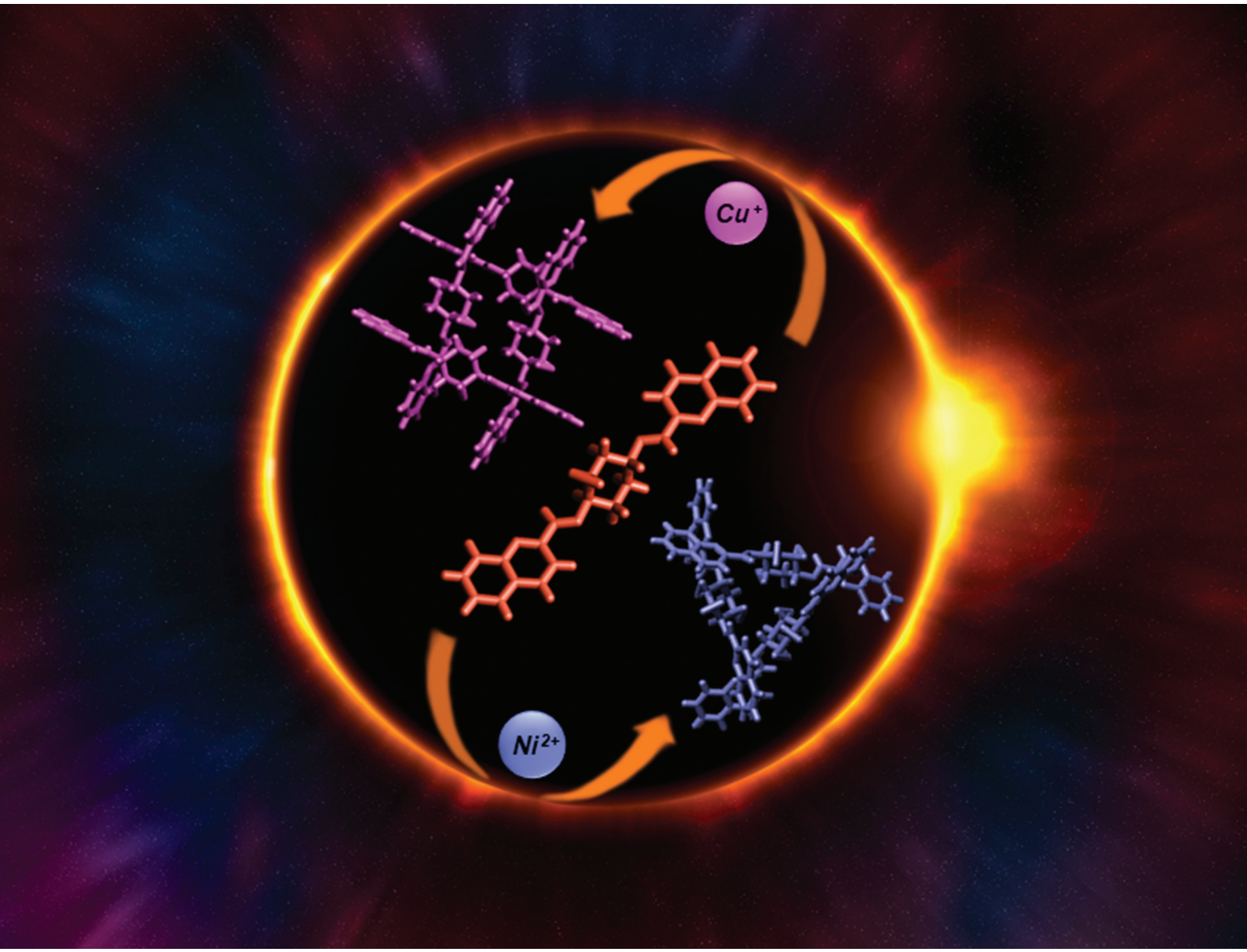

ISSN 1477-9226

ROYAL SOCIETY OF CHEMISTRY

PAPER

Marta A. Fik-Jaskółka *et al.*

New Cu(I) square grid-type and Ni(II) triangle-type complexes: synthesis and characterization of effective binders of DNA and serum albumins

Dalton Transactions

ROYAL SOCIETY OF CHEMISTRY

PAPER

View Article Online
View Journal | View Issue

Check for updates

Cite this: *Dalton Trans.*, 2022, **51**, 15648

New Cu(I) square grid-type and Ni(II) triangle-type complexes: synthesis and characterization of effective binders of DNA and serum albumins†‡

Martyna Szymańska,[a] Maciej Kubicki, [a] Giovanni N. Roviello, [b] Giuseppe Consiglio, [c] Marta A. Fik-Jaskółka *[a] and Violetta Patroniak [a]

Received 13th July 2022,
Accepted 31st August 2022

DOI: 10.1039/d2dt02271k

rsc.li/dalton

Multivalent molecules are a potential group of bioactive compounds endowed with high affinity and specificity in innovative biomolecule-targeting therapeutic approaches. Herein, we report on a new and versatile N,N,N,N-donor ligand L (1*R*,4*R*)-N1,N4-bis(quinolin-2-ylmethylene)cyclohexane-1,4-diamine with two coordinating quinoline moieties connected with *trans*-1,4-diaminocyclohexane. It coordinates Cu^{+} forming a [2 × 2] square grid-type complex **C1** $[Cu_4L_4]^{4+}$ and Ni^{2+} giving a triangle-type complex **C2** $[Ni_3L_3]^{6+}$. We screened their potential as versatile metal-based Serum Albumin (SA), double helical and G-quadruplex DNA binders taking advantage of their shape, size and stability effects using different spectroscopic experiments (UV-Vis, fluorescence, circular dichroism). The findings of our work suggest the potential utility of the metal complexes herein described in the context of the new drug discovery.

Open Access Article. Published on 13 October 2022. Downloaded on 2/5/2023 3:04:53 PM.
This article is licensed under a Creative Commons Attribution 3.0 Unported Licence.

Introduction

The molecular self-assembly driven by the coordination of metal ions is a powerful tool providing access to a wide variety of metal complexes with extensive applications in host–guest chemistry,[1] biomedicine,[2] catalysis,[3] electrooptical devices[4,5] and magnetism.[6] Owing to the wide range of ligands and metals compatible with the principles of supramolecular chemistry a wide range of discrete coordination complexes, including two- (2D) and three-dimensional (3D) architectures, with well-defined shapes and sizes has been emerged over the last years.[7–9] Metal-based supramolecular scaffolds offer unique advantages over conventional organic molecules in the targeting of biorelevant molecules (proteins, nucleic acids) due to the stereochemical and geometrical diversity conferred through the metallic centre.[10] In fact, the vital life processes heavily rely on the recognition phenomena between the relatively simple precursors folding into complex matter and became the paradigm of the supramolecular chemistry.[9] The self-assembly can be achieved through the utilization of the directional H-bonding or other non-covalent interactions such as van der Waals, ion-ion, ion-dipole, π–π stacking and hydrophobic interactions. It can be also realized by the dynamic, predictable and directional coordination bonding. So far, a wide array of 2D grids, triangles, rectangles, helicates, 3D cubes, trigonal pyramids, adamantoids and other cages synthesized by this approach have been reported.[11,12]

As mentioned above, the rational design empowers formation of aesthetically appealing architectures with functional applicability. The well-defined and thermodynamically stable scaffolds are of particular interest for their potential anticancer properties attained through various mechanisms. The metallo-supramolecular complexes-based drugs can be used in two main strategies – directly as drugs or as carriers for the drugs.[13]

Metallo-supramolecular complexes, both old and new, are currently being evaluated in conjunction with spectroscopic and biological techniques to probe their interactions with DNA and proteins, the relevant biomolecules. For this purpose, the metal ions are mainly used as core structural units, while the surrounding ligands are used for the binding with target molecules. Using the metal ions in a structural sheath allows for their use in cells, since the metals are unable to non-specifically coordinate to biomolecules and exert the toxic effect.[10] A variety of biological interactions can be expected given the diversity of ligands. The interactions with negatively-charged DNA can arise due to the subtle non-coordinate interactions, such as electrostatic attraction on the surface of the helix,

[a]*Faculty of Chemistry, Adam Mickiewicz University, Uniwersytetu Poznańskiego 8, 61-614 Poznań, Poland. E-mail: martafik@amu.edu.pl*
[b]*Institute of Biostructures and Bioimaging – CNR, Area di Ricerca site and Headquartes, Via Tommaso De Amicis, 95, 80145 Napoli, Italy*
[c]*Dipartimento di Scienze Chimiche, Università degli studi di Catania, viale A. Doria 6, I-95125 Catania, Italy*

† Dedicated to Professor Paolo Finocchiaro on the occasion of 80th birthday.

‡ Electronic supplementary information (ESI) available. CCDC 2097988–2097990. For ESI and crystallographic data in CIF or other electronic format see DOI: https://doi.org/10.1039/d2dt02271k

This journal is © The Royal Society of Chemistry 2022

Open Access Article. Published on 13 October 2022. Downloaded on 2/5/2023 3:04:53 PM.
This article is licensed under a Creative Commons Attribution 3.0 Unported Licence.

intercalation, groove binding as well as combination of all these modes.[10,14,15] The double helix of DNA is a carrier of genetic information, therefore it is relevant from the therapeutic viewpoint, since the malfunction of DNA-related processes may lead to cells death and suppression of the tumor growth.[16] The formation and stabilization of the GQ in the human telomeric sequences has also been shown to inhibit the activity of telomerase, a cancer-specific reverse transcriptase that is activated in 80–90% of tumors.[17] Thus, the telomeric DNA GQ has been considered to be an attractive target for cancer therapeutic intervention.[18–20]

A therapeutic effect consists not only from the actual mechanism of the impairment of the processes in cancer cells but also from the transportation strategy. An important group of biomolecules are SA which act as the most significant modulators of plasma oncotic pressure and functions to transport a variety of substances. The ligands transported by SA include the endogenous ions, fatty acids, bilirubin, and the exogenous drugs as methotrexate, paclitaxel, warfarin, methadone, furosemide, and many others.[21,22] The non-immunotoxicity, long circulation times and high accumulation in tumors are the attributes making SA good anticancer drug carriers.[23] The SA are predominately present in the extravascular space rather than in intravascular. They return from the extravascular space into circulation through the lymphatic system.[24] Since the solid tumors commonly possess an immature, highly permeable vasculature and lack the sufficient lymphatic drainage[25] they tend to accumulate the macromolecules (as SA) within the tumor interstitium (it is known as the enhanced permeation and retention effect).[26] This mechanism is used by the cancer cells to use albumin as the source of nutrients to sustain cancer cell proliferation.[27] The same pathway can also be used for the drug delivery protocol bound to SA. Therefore, investigating the mechanism of binding of bioactive compounds with SAs is of a clear interest in the design of new anticancer molecules, to be used in targeted therapy and of their efficient delivery systems.

So far Drożdż *et al.* have showed the potency of multivalent cationic supramolecular Zn(II) grids as DNA binders.[28,29] Domarco *et al.*[30] demonstrated the usefulness of metal-directed self-assembly (MDSA) strategy for the rapid access of a family of square-shaped metallacycles of different sizes binding the unique pocket of the c-kit oncogene, an important target in the treatment of gastrointestinal tumors.[31] Moreover, just in 2021 Zhang *et al.* presented a Pt(II) based metallatriangle inducing the PDT effect through ROS generation.[32]

Here we present a study on the design and synthesis of the metalosupramolecular multivalent square grid-type complex **C1** $[Cu_4L_4]^{4+}$ and a triangle-type complex **C2** $[Ni_3L_3]^{6+}$ where **L** is a chameleonic ditopic N,N,N,N-donor ligand N,N-bis(quinolin-2-ylmethylene)cyclohexane-1,4-diamine. The compounds were characterized by NMR, ESI-MS, EA and X-ray diffraction of monocrystals. Next, keeping in mind the multivalency of the complexes, we decided to study their potential for the binding with biorelevant molecules as DNA and Serum Albumin (SA) using some spectroscopic techniques (UV-Vis absorption, fluorimetry, circular dichroism).

Results and discussion

Concept, synthesis, characterization and stability of compounds

One of the advantages provided by supramolecular chemistry is obtaining a precisely chosen output from the input data. Another important parameter is the stability of the output figures, since it is directly translated onto their possible *in vivo* applications. At the same time the decomposition of compounds in certain conditions is desirable for the drug release in cells. As revealed before[33–36] the properly designed Schiff base ligands may be suitable for the formation of various supramolecular scaffolds. Therefore, herein, we report on a specific assembly of a supramolecular square grid-type and triangle-type complexes from the tetradentate N,N,N,N-donor Schiff base ligand **L** N,N-bis(quinolin-2-ylmethylene)cyclohexane-1,4-diamine and metal ions Cu(I) and Ni(II), respectively. Ligand **L** was obtained by an efficient condensation reaction of 2 equiv. of 2-quinolinecarboxaldehyde with 1 equiv. of *trans*-1,4-diaminocyclohexane (Fig. S1‡). It was designed so as to possess two N,N-donor moieties separated by the cyclohexane ring. Such separator is rigid enough to play a role of the side wall of the molecular geometrical figures. As depicted in Fig. 3 (*cf.* 3.2.) a free ligand **L** exists as transoid conformer in solid state, while in complexes it can adopt, as expected, both cisoid and transoid conformation influencing the final complex arrangement.[37–40] As revealed by X-ray diffraction method (*cf.* 3.2.) the complexation of 1 equiv. of Cu(I) ions results in the formation of a square grid-type complex **C1** ($[Cu_4L_4]^{4+}$) with two parallel ligands in a cisoid conformation and the other two as transoid isomers, while complexation of Ni(II) ions gives a triangle-type complex **C2** ($[Ni_3L_3]^{6+}$) with transoid conformers of **L** (Scheme 1).

The reaction of **L** and Cu(I) is very selective as it leads to a single product – a [2 × 2] square grid-type complex **C1**. In ESI-MS spectrum of the **C1** a characteristic peak appears at m/z = 2259 for $\{[Cu_4L_4](PF_6)_3\}^+$ (Fig. S2‡), while for the triangle-type complex **C2** only a part of the complex is visible at m/z = 459 for $[NiL(ClO_4)]^+$ (Fig. S3‡). Also the peaks at m/z = 393 and 415 for $[HL]^+$ and $[NaL]^+$ are present probably because of decomposition of the complex during ionization. The NMR titration

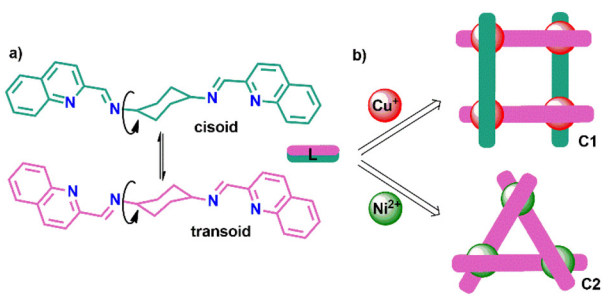

Scheme 1 (a) Conformational isomerism of ligand **L**; (b) schematic demonstration of the formation of complexes **C1** and **C2** (the counter-ions in **C2** where omitted for clarity).

Open Access Article. Published on 13 October 2022. Downloaded on 2/5/2023 3:04:53 PM.
This article is licensed under a Creative Commons Attribution 3.0 Unported Licence.

experiment revealed that the [2 × 2] square grid-type complex **C1** forms selectively among other possible products and that even excess of Cu(I) does not lead to complexes of different ratios (Fig. 1). During titration, ^{1}H NMR spectra show a progressive shifting of the peaks due to the formation of the complex, especially prominent for the signal of imine proton –CH═N– which is very close to the binding site of the ligand.

The UV titration of ligand **L** with $Cu(MeCN)_4PF_6$ and $Ni(ClO_4)_2{\cdot}6H_2O$ confirmed the formation and stabilization of the square grid-type structure of **C1** and the triangle-type structure of **C2** in acetonitrile. In both cases three isosbestic points were observed: at 298, 260 and 250 nm for **C1** and at 305, 265 and 250 nm in case of **C2**. Importantly, no more changes in the UV-Vis spectrum is visible after addition of 1 equiv. and 1.33 equiv. of Cu(I) and Ni(II), respectively. (Fig. 2).

The aim of this work was understanding the abilities of multivalent square grid-type complex **C1** ($[\mathbf{Cu_4L_4}]^{4+}$) and triangle-type complex **C2** ($[\mathbf{Ni_3L_3}]^{6+}$) to interact with some biomedically-relevant macromolecules – such as DNA and proteins, using Bovine Serum Albumin (BSA) as a model. Before performing the spectroscopic experiments, we evaluated the stability of the compounds within 2 hours (the time period was correlated with the duration of experiments) in the appropriate buffers. While the spectrum of ligand **L** seemed unchanged over time, the spectrum of **C1** underwent subtle hypochromic changes related, according to our hypothesis, to the exchange of the outer coordination sphere of metal ions for the ligands abundant in the buffer (chlorides, hydroxyl, aqua *etc.*) leaving the grid scaffold undisrupted. Importantly, the stock solutions of **C1** remain red for several weeks suggesting that the coordinated metal ions do not oxidize easily. Similarly, the triangle-type complex **C2** seemed to exchange the outer coordination sphere, but also the inner labile ligands (acetonitrile molecules) for the other being abundant in the buffer solutions (Fig. S4 and S5‡). The lower stability of the more constrained structure of **C2**, in comparison to the structure of **C1**, found also reflection in the ESI-MS spectra reported above.

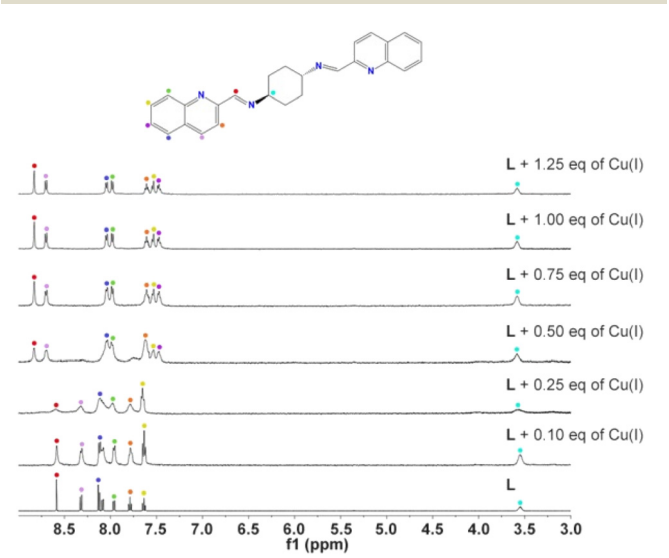

Fig. 1 Titration of ligand L (5×10^{-4} M in CD_3CN) with $Cu(CH_3CN)_4BF_4$ (5×10^{-3} M in CD_3CN) at 27 °C. The titration was performed with $Cu(MeCN)_4BF_4$ instead of $Cu(MeCN)_4PF_6$ due to the better solubility of this salt in MeCN.

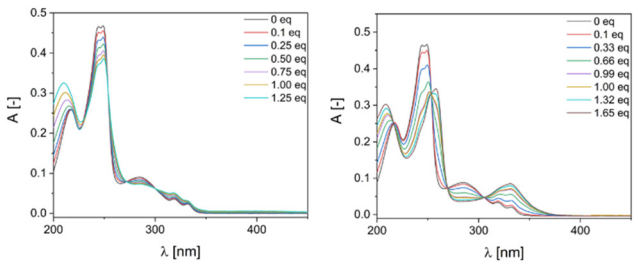

Fig. 2 UV-Vis titration spectra of ligand in MeCN (5.1 μM) with (left) $Cu(MeCN)_4PF_6$ (0–1.25 equivalents of Cu(I)) and (right) $Ni(ClO_4)_2{\cdot}6H_2O$ (0–1.65 equivalents of Ni(II)).

Description of the crystal structures

Perspective views of the molecule **L**, and cations from the structures **C1** and **C2** are shown in Fig. 3. The ligand molecule in the crystal structure is C_i-symmetrical as it lies across the inversion center in the space group $P2_1/c$; as a consequence, the two symmetry-related quinoline ring systems are exactly parallel. It is potentially tetradentate (N_4) and in such denticity it exists in the Cu and Ni complexes **C1** and **C2**.

The crystal structures of two cationic complexes show the flexibility of the ligand and its potential to create different architectures. The Cu(I) complex, **C1**, exists as the C_i-symmetrical, four-centered $Cu_4L_4^{4+}$ tetra-cation, with 4-coordinated Cu ions in the severely distorted tetrahedral environment (Table S1‡ lists the relevant geometrical data). In agreement with the requirements of this certain architecture the quino-

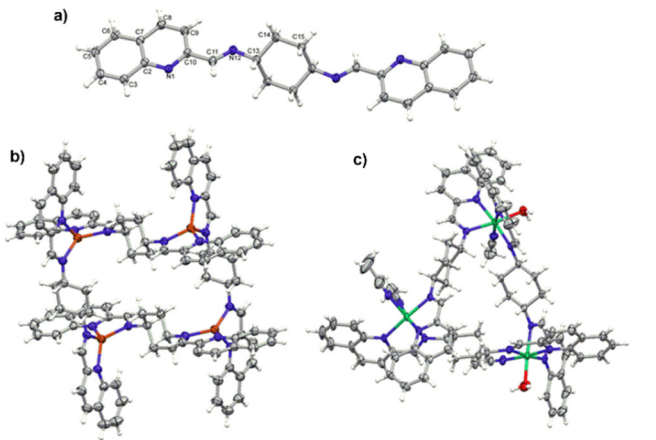

Fig. 3 (a) Perspective view of the ligand **L**. The unlabeled part of the molecule is related to the labelled one by symmetry operation 1–*x*, 2–*y*, 1–*z*; (b) perspective view of the square grid-type complex **C1**; (c) perspective view of the triangle-type complex **C2**. All ellipsoids are drawn at the 50% probability level; hydrogen atoms are shown as spheres of arbitrary radii.

This journal is © The Royal Society of Chemistry 2022

Open Access Article. Published on 13 October 2022. Downloaded on 2/5/2023 3:04:53 PM.
This article is licensed under a Creative Commons Attribution 3.0 Unported Licence.

line planes are almost parallel (*cf.* dihedral angles in Table S1‡).[37–40] In turn, Ni(II) complex **C2** makes triangular three-centered Ni_3L_3 structures, in which the Ni centers are six-coordinated in the quite regular octahedral geometry. As such a geometry requires additional ligands, the complex uses the solvent molecules. One of the Ni cations is additionally coordinated by two acetonitrile molecules (effectively N_6), while the other two by one acetonitrile and one water molecule (N_5O). In this case the particular geometry requires more twisted ligand conformation, and appropriately the dihedral angles between terminal quinoline rings are much larger.

The crystal structures also contain counterions and solvent molecules. In **C1** there are four quite well-determined PF_6 anions, four acetonitrile molecules and two toluene molecules, situation of **C2** seems to be more complicated. The crystal structure suggests that besides the perchlorate anions (effectively 5.5), the half-occupied (at the inversion center), well-defined C_i-symmetrical octahedral anion is present; it has been interpreted as the PF_6^-, a result of the impurities. Additionally, one CH_3CN and a number of at least partially occupied, disordered water molecules were found in this crystal structures.

Interestingly, even though a number of anions and water molecules were found, the structures are still quite porous, with the voids (up to 10% of the unit-cell volume) filled with the diffused solvent molecules.

DNA models as targets

The utilization of non-classical interactions of small molecules with nucleic acids can modulate the cellular interactions related to DNA and are of value as they manipulate the function of cells to produce a desired result, thereby allowing the diagnosis and/or treatment of disease.[41,42] The spectroscopic properties of metal ions make them ideal not only from the design viewpoint, as scaffolds, but also as active sites.[43] In our preliminary studies we employed several spectroscopic techniques to understand the interactions between the supramolecular Cu^+ square grid-type complex **C1** and Ni^{2+} triangle-type complex **C2** with a duplex DNA and the GQ forming sequence Tel22 as a lower cost alternative for Pt^{2+} and Ru^{2+} compounds.

First, in our study we investigated the affinity of **C1**, **C2** and **L** toward the double helical DNA with use of absorption titration experiments (Fig. 4, Fig. S6‡). While **C2** and **L** exhibited only weak interactions with the CT-DNA, the square grid-type complex **C1** has shown to be a good DNA binder of a high affinity expressed in the binding constant $K_b = 1.38 \times 10^6$; the standard Gibb's free energy is equal to -34.46 kJ mol^{-1}.

Since such a large K_b suggests intercalation[14] the competitive fluorescence quenching experiments with ethidium bromide (a classical intercalator) were conducted. As could be inferred, only the **C1** pushed out the ethidium bromide from its fluorescent complex with DNA (Fig. 5a and Fig. S7‡). The interaction is expressed by the Stern–Volmer quenching constant equal to $K_{SV} = 7.12 \times 10^4$. The intercalation mode of binding has been further confirmed by the UV-thermal melting experiments which showed the stabilization of double helix by *ca.* 4 °C (Fig. 5b, Fig. S8 and S9‡).

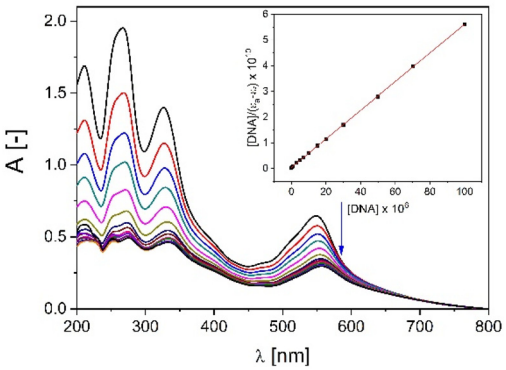

Fig. 4 Absorption titration of **C1** with increasing concentrations of CT-DNA (0–100 μM) in buffer Tris-HCl (5 mM Tris, 50 mM NaCl, pH = 7.22). Arrow shows hypochromic changes upon increasing CT-DNA concentration. Inset: plot of [DNA]/($\varepsilon_a - \varepsilon_f$) *versus* [DNA]; ■, experimental data points; solid line, linear fitting of the data.

The intercalation describes the reversible insertion of a flat guest molecule into a lamellar host structure. DNA-drug intercalation is typically stabilized by significant π–π stackings, hydrophobic and polar interactions, as well as the electrostatic forces of cationic intercalators with polyanionic nucleic acid.[44] By taking a closer look at the structure of cationic **C1** one can type it is a potential example of a bis-intercalator due to its structural analogy to the bisantracyclines containing two daunorubicin molecules separated by 7 Å by a *p*- and *m*-xylylenyl linkers. Additionally, the linkers of the two daunorubicines line the minor groove of DNA. Such an arrangement on the two opposite sides of the metallogrid potentially could also allow it to cross-intercalate the DNA helixes (Fig. 5c). In our case the stiffened cyclohexane could also, potentially, interact on the surface of the helix and, moreover, the metal ions incorporated in the scaffold can induce the electrostatic interactions.[45]

Stabilization of GQ forming sequences to prevent its disassembly is a target of many studies[30,46,47] therefore, taking advantage of the multivalency of metallosupramolecular complexes, we performed preliminary GQ binding (Fig. S10‡) and induction (induced circular dichroism, ICD) experiments (Fig. S10 and S11‡). Interestingly, the ICD spectra (the spectra given by the randomly folded Tel22 incubated with the given compound minus randomly folded Tel22, all in the absence of K^+) suggest that the triangle-type complex **C2** could induce a structure formation in the randomly folded telomeric Tel22 sequence (that is able to form hybrid type GQ in K^+ solutions, Fig. S11‡), while **C1** does not have any effect on the random DNA structure (Fig. S12‡). The final assembly is characterized by a spectrum with positive peaks at *ca.* 240 nm and 280 nm and negative peaks at *ca.* 260 nm and 300 nm (Fig. S10‡).[48]

Protein model as a target

Since the SA is a negatively charged protein it seemed to be reasonable to evaluate the cationic metallo-supramolecular square grid-type complex **C1** (charge 4+) and triangle-type

Open Access Article. Published on 13 October 2022. Downloaded on 2/5/2023 3:04:53 PM.
This article is licensed under a Creative Commons Attribution 3.0 Unported Licence.

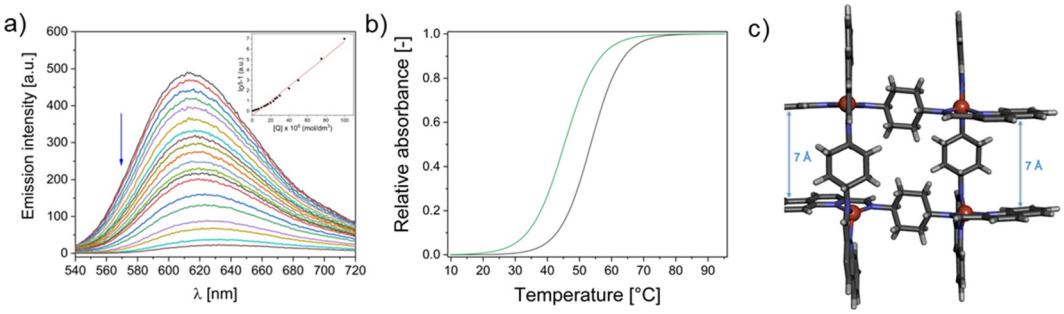

Fig. 5 (a) Emission spectra of ethidium bromide bound to CT-DNA in the presence of increasing amounts of **C1** (0–200 μM) in buffer Tris-HCl (5 mM Tris, 50 mM NaCl, pH = 7.22). Arrow shows the hypochromic changes upon increasing concentration of **C1**; inset: Stern–Volmer plot of $I_0/I - 1$ *vs.* [**C1**] for the titration of EtBr-CT-DNA complex; ■, experimental data points; solid line, linear fitting of the data. (b) UV thermal melting curves of d(GTTAATCGCTGG) alone (green line) and with 4 eq. of **C1** (black line) in cacodylate buffer (10 mM sodium cacodylate, 100 mM sodium chloride, pH = 7.23); DNA concentration is equal to 2.5 μM. (c) Structural conditions of **C1** to act as bis-intercalator. Two parallel pairs of quinolines in transoid conformers of **L** are 7 Å apart.

complex **C2** (charge 6+) as binders. In our study we used BSA, since it is the most commonly used albumin model in *in vitro* experiments due to its similarity (76%) to Human Serum Albumin (HSA).[49] The binding propensity of **C1**, **C2** and **L** toward BSA was studied by fluorescence and CD spectroscopy. Due to the presence of neutral amino acids such as Trp, Tyr and Phe, the BSA protein shows a high fluorescence. The gradual diminution of the fluorescence band arising from the Trp-214 residue upon addition of potential drugs was monitored (Fig. 6) which suggest that they interact with the hydrophobic pocket of domain II. Analysis of the Stern–Volmer plots has shown that the square grid-type complex **C1** ($K_{SV} = 8.0 \times 10^4$), triangle-type complex **C2** ($K_{SV} = 1.1 \times 10^5$) and ligand **L** ($K_{SV} = 2.3 \times 10^4$) bind the BSA. The quenching rate k_q was the highest for the **C2** (1.1×10^{13} dm^3 (mol s)$^{-1}$, while for **C1** and **L** it was and $k_q = 8.0 \times 10^{12}$ dm^3 (mol s)$^{-1}$ and $k_q = 2.3 \times 10^{12}$ dm^3 (mol s)$^{-1}$, respectively. One may assume it is due to the highest positive charge of triangle-type complex **C2** equal to 6+. The affinity of our compounds toward BSA was characterized with the Scatchard method (Table 1, Fig. 7). While all compounds have similar number of binding sites (n) on BSA (*ca.* 1.0), **C1** has a high K_b of *ca.* 10^6 and **L** a low K_b of *ca.* 10^3. Since the high K_b of drug–protein interaction can cause problems with release of the drug in the target region, the most moderate K_b of **C2** equal to 10^5 seems to be the most promising in terms of the effective transportation and release to the tumor site by carrier proteins as SA.

Also, the conformational changes of BSA occurring upon binding were observed in the titration monitored by CD which is a precise and sensitive technique for the studies on secondary structures of proteins (Fig. 8). The bands at 209 nm (arising from n–π* transitions) and at 222 nm (from π–π* transitions) are characteristic for the α-helical structure of the BSA protein (*ca.* 55%).[50,51] The high K_b of square grid-type complex **C1** correlates well with the CD spectrum of BSA titrated with **C1** in which an α-helix content dramatically drops to finally reach only 6%. Such distortion is undesirable, since they may

Table 1 Number of binding sites (n) and binding constant (K_b) for **C1**, **C2** and ligand **L** with BSA

Compound	n	K_b
C1 $[Cu_4L_4]^{4+}$	1.2	1.9×10^6 ($R^2 = 0.99$)
C2 $[Ni_3L_3]^{6+}$	1.0	4.1×10^5 ($R^2 = 0.97$)
L	0.8	5.2×10^3 ($R^2 = 0.99$)

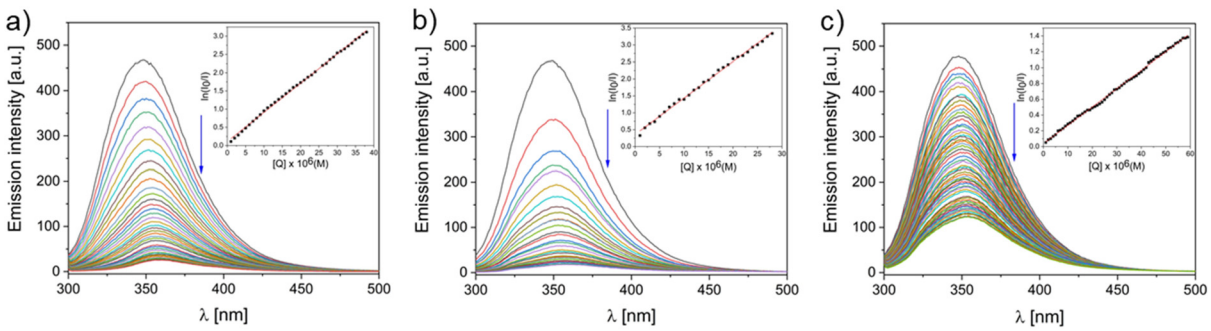

Fig. 6 Fluorescent BSA (5 μM) titration with increasing concentrations of **C1** [0–38 μM, (a)], **C2** [0–28 μM, (b)] and **L** [0–59 μM, (c)] in PBS buffer (0.01 M phosphate buffer, 0.0027 M potassium chloride, 0.137 M sodium chloride pH = 7.4). Inset: plot of $\ln(I_0/I)$ *vs.* [Q]; ■, experimental data points.

This journal is © The Royal Society of Chemistry 2022

Open Access Article. Published on 13 October 2022. Downloaded on 2/5/2023 3:04:53 PM.
This article is licensed under a Creative Commons Attribution 3.0 Unported Licence.

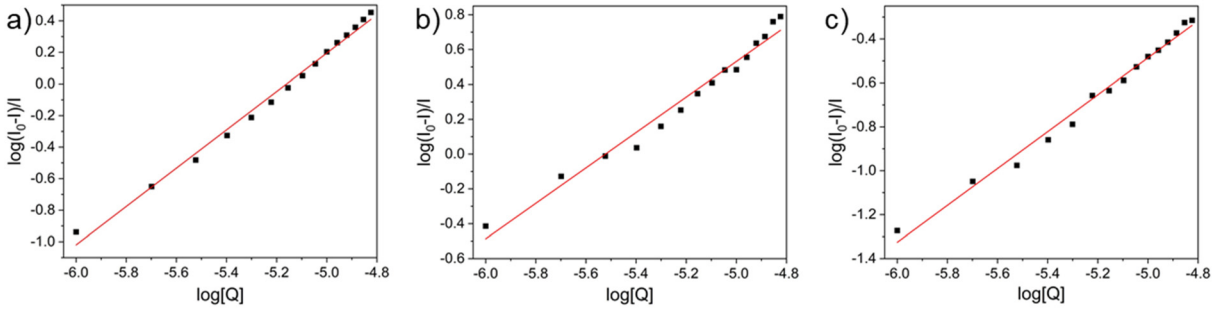

Fig. 7 Scatchard plot of titration of BSA (5 μM) with **C1** [0–15 μM, (a)], **C2** [0–15 μM, (b)] and **L** [0–15 μM, (c)] in PBS buffer (0.01 M phosphate buffer, 0.0027 M potassium chloride, 0.137 M sodium chloride pH = 7.4).

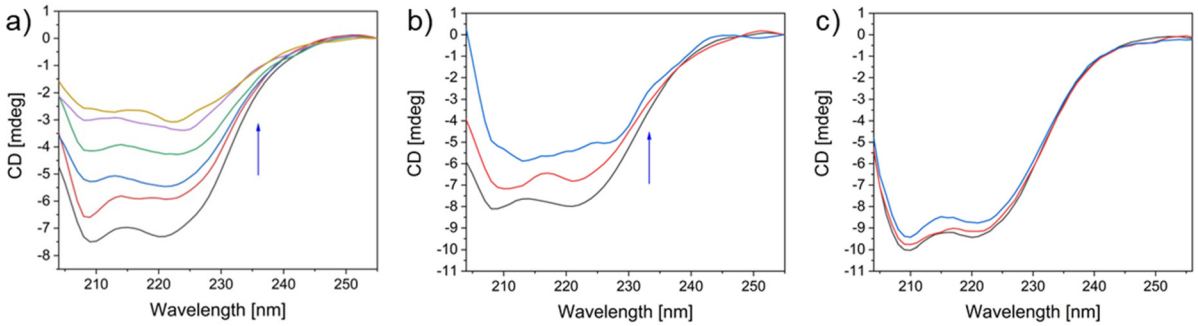

Fig. 8 CD spectra of BSA (75 nM) in the presence of increasing concentration of **C1** [0–37.50 μM, (a)], **C2** [0–15.00 μM, (b)] and **L** [0–15.00 μM, (c)] in PBS buffer (0.01 M phosphate buffer, 0.0027 M potassium chloride, 0.137 M sodium chloride pH = 7.4).

lead to the impairment of the protein's functions. On the contrary, **L** was almost neutral for the BSA structure, while the triangle-type complex **C2** moderately influenced the structure of BSA (decrease of α-helix content to 25%). Thus, together with its moderate K_b, one may assume it is able to be efficiently transported by SA.

Conclusion

In conclusion, we were able to synthesize the [2 × 2] square grid-type complex **C1** $[\mathbf{Cu_4L_4}]^{4+}$ and triangle-type complex **C2** $[\mathbf{Ni_3L_3}]^{6+}$ with interwoven chameleonic N,N,N,N-donor ligand **L** as confirmed by X-ray. The versatility of such metallosupramolecular constructs prompted us to screen their specific interactions with relevant biomolecules – double stranded DNA, GQ and SA protein by means of several spectroscopic methods (UV-Vis absorption, fluorescence, circular dichroism). While the ligand **L** shows rather low affinity toward the tested molecules, we revealed that the square grid-type complex **C1**, possessing two parallel transoid ligands, attaches to the SA causing serious reduction of the α-helix content in the peptide and, according to our spectroscopic studies, intercalates double stranded DNA. On the other hand, the triangle-type complex **C2** moderately binds SA and causes smaller structural perturbations in the peptide structure and also seems to induce a secondary structure in the unfolded GQ-forming sequence of Tel22. As a result, this preliminary study underlines the potential of multivalent metallo-supramolecular complexes in comparison to the free ligands in future drug design.

Experimental

Materials and physical measurements

CT-DNA, BSA, ethidium bromide, Tris, PBS, metal salts and NaCl were supplied from Merck and used without further purification. Tel22 (d[AGGGTTAGGGTTAGGGTTAGGG]) was supplied from Genomed S. A. (Warsaw). ESI mass spectra for H_2O solutions ~10^{-4} M were measured using a Waters Micromass ZQ spectrometer. NMR spectra were run on a Varian Gemini 300 MHz (for ligand) or Mercury-plus 400 MHz (for **C1**) spectrometer and were calibrated against the residual protonated solvent signals with chemical shifts represented in ppm. Microanalyses were performed using Vario EL III CHN element analyzer. The FT-IR spectra were recorded in the range between 400 and 4000 cm^{-1} using Bruker FT-IR IFS 66 s^{-1} spectrometer. CT-DNA was dissolved in Tris Buffer (5 mM Tris HCl, 50 mM NaCl, pH 7.3) prior to use. The CT-DNA solution gave a ratio of UV absorbance of 1.82 : 1 at 260 and 280 nm, indicating that the CT-DNA sample was sufficiently free from protein.[52,53] CT-DNA concentration per nucleotide was determined from the UV absorbance at 260 nm using the extinction coefficient ε_{260} = 6600 dm^3 mol^{-1} cm^{-1}.[54] BSA solution was

Open Access Article. Published on 13 October 2022. Downloaded on 2/5/2023 3:04:53 PM.
This article is licensed under a Creative Commons Attribution 3.0 Unported Licence.

prepared at a 75 nM concentration based on its molecular weight (MW 66 kDa) using PBS ([NaCl]: 137 mM; [KCl]: 2.7 mM; [Na_2HPO_4]: 10 mM; [KH_2PO_4]: 1.8 mM; pH 7.3) as a solvent for the spectral experiments. Additionally, BSA solution was checked spectroscopically and stored in the dark environment at 4 °C before usage. Electronic absorption titrations and melting experiments were performed on JASCO V-770 spectrophotometer equipped with a Peltier-thermo Cell Holder (water) PAC743R, in 10 × 10 mm quartz cells. Emission spectra in the competitive fluorescence titration experiments were measured at room temperature on an Agilent Technologies G9800A spectrofluorimeter in the range 540–720 nm with excitation and emission slits of 10 nm and excitation wavelength λ_{exc} = 467 nm in 10 × 10 mm quartz cells. CD spectra of BSA were obtained on a J-810 spectropolarimeter (Jasco Europe S.R.L., Cremella, Italy) equipped with a Peltier PTC-423S/15, using a Hellma (Milan, Italy) quartz cell (10 mm). In the investigation of BSA the spectra were measured in the 204–255 nm wavelength range at 15 °C. Freshly prepared stock solutions of complexes in MeCN [at concentration 5×10^{-3} M (for CD measurements) or 2×10^{-3} M (for other measurements)] were taken for all spectroscopic investigations.

Synthesis of ligand L N,N-bis(quinolin-2-ylmethylene) cyclohexane-1,4-diamine

trans-1,4-Diaminocyclohexane (51.80 mg, 0.45 mmol) was dissolved in 6 ml of $EtOH_{abs}$. Then 2-quinolinecarboxaldehyde (2 equiv., 142.59 mg, 0.90 mmol) was added. The reaction was carried out in inert conditions with heating under reflux for 3 hours and then left for 21 hours at room temperature. The solution became brown and after a while a cream-colored precipitate formed. The solution was concentrated and the precipitation was filtered under reduced pressure. The precipitate was washed with cold $EtOH_{abs}$. Yield 81.58% (Scheme 2).

^{1}H NMR (300 MHz, DMSO-d_6): δ (ppm) = 8.60 (s, 1H); 8.44 (d, 1H); 8.07 (m, 3H), 7.82 (t, 1H); 7.67 (t, 1H); 1.82 (dt, 4H).

^{13}C NMR (75 MHz, DMSO-d_6): δ (ppm) = 160.47; 154.67; 147.24; 136.9; 130.16; 129.16; 128.36; 128.13; 127.65; 117.95; 67.84; 32.08 (2C).

ESI-MS(+) *m*/*z* (%): 393 (78) $[HL]^+$; 254 (43) $[HA]^+$; 415 (90) $[L + Na]^+$; 807 (100) $[2L + Na]^+$.

FT-IR (ATR): 3037 ν(C–H)$_{arom}$; 2928, 2858 ν_s(C–H)$_{aliphatic}$; 1642, 1596 ν(C=C); 1463, 1449 ν(C=N); 1085, 986, 957, 943, 9905, 791, 778, 757, 618 γ(C–H)$_{arom}$ cm^{-1}.

Anal. calcd for ($C_{26}H_{24}N_4$): C: 79.56, H: 6.17, N: 14.27%; found: C: 78.92, H: 6.11, N: 14.37%.

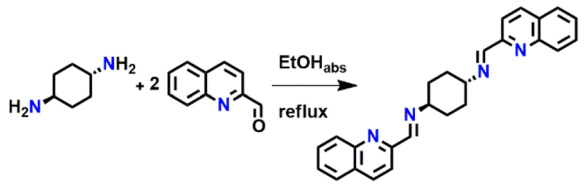

Scheme 2 Synthesis of ligand (L).

Synthesis of complex C1

The ligand **L** (21.00 mg, 0.053 mmol) was dissolved in 10 ml of MeCN giving a yellow solution. Then the $Cu(MeCN)_4PF_6$ salt (1 equiv., 19.94 mg, 0.053 mmol) was added and the solution turned into dark purple. The reaction was carried out for 24 hours. Then the solution was concentrated to *ca.* 2 ml on a rotary evaporator and 2 ml of Et_2O were added. The dark purple precipitate formed was filtered under reduced pressure. Yield: 13.78%.

A dark purple single crystal suitable for X-ray studies was obtained by a slow vapour diffusion of MeCN from the solution of complex $\mathbf{[Cu_4L_4]^{4+}}$ to toluene.

^{1}H NMR (400 MHz, CD_3CN-d_6): δ (ppm) = 8.83 (s, 1H); 8.70 (d, 1H); 8.04 (d, 1H), 7.98 (d, 1H); 7.61 (t, 1H); 7.53 (d, 1H); 7.47 (t, 1H); 3.58 (s, 1H); 1.57 (m, 4H).

ESI-MS(+) *m*/*z* (%): 2259.72 (90) $\{[Cu_4L_4](PF_6)_3\}^+$; 1057.29 (85) $\{[Cu_4L_4](PF_6)_2\}^{2+}$; 656.84 (100) $\{[Cu_4L_4](PF_6)\}^{3+}$; 456.38 (30) $[Cu_4L_4]^{4+}$.

FT-IR (ATR): 3060 ν(C–H)$_{arom}$; 2932, 2860 ν_s(C–H)$_{aliphatic}$; 1622, 1590 ν(C=C); 1455, 1434 ν(C=N); 1092, 1019, 996, 935, 783 γ(C–H)$_{arom}$; 833, 750 (PF_6^-)cm^{-1}.

Anal. calcd for $[(C_{104}H_{92}Cu_4N_{16})^{4+}\cdot 4(PF_6)^-\cdot 6(C_2H_3N)]$: C: 52.65, H: 4.19, N: 11.64%; found: C: 52.13, H: 4.22, N: 11.56%.

Synthesis of complex C2

The ligand **L** (21.23 mg, 0.054 mmol) was dissolved in 10 ml of MeCN giving a yellow solution. Then the $Ni(ClO_4)_2\cdot 6H_2O$ salt (1 equiv., 19.78 mg, 0.054 mmol) was added, the solution turned cloudy yellow-orange. The reaction was carried out for 24 hours. Then the solution was concentrated to *ca.* 2 ml on a rotary evaporator and 1 ml of Et_2O was added. The brown precipitate formed was filtered under reduced pressure. Yield: 22.76%.

A brown single crystal suitable for X-ray studies was obtained by a vapour slow diffusion of i-Pr_2O into a solution of complex $\mathbf{[Ni_3L_3]^{6+}}$ in MeOH and MeCN (1 : 1 in volume).

ESI-MS(+) *m*/*z* (%): 393 (100%) $[L + H]^+$; 449 (35) $[L - H + Ni]^+$; 512 (30) $[L + NiCO_3]^+$; 549 (25) $[L + NiClO_4]^+$; 904 (5) $[2L + NiCO_3]^+$; 941 (5) $[2L + NiClO_4]^+$.

FT-IR (ATR): 3082 ν(C–H)$_{arom}$; 2944, 2868 ν_s(C–H)$_{aliphatic}$; 1618, 1593 ν(C=C); 1466, 1436 ν(C=N); 1000, 958, 950, 931, 904, 801, 772, 753 γ(C–H)$_{arom}$; 1060; 620 (ClO_4^-) cm^{-1}.

Anal. calcd for $[2(C_{86}H_{88}N_{16}Ni_3O_2)^{6+}\cdot 11(ClO_4)^-\cdot Cl^-\cdot 2(C_2H_3N)\cdot CH_4O\cdot 7H_2O]$: C: 47.48, H: 4.50, N: 10.64%; found: C: 46.34, H: 4.54, N: 10.73%.

X-ray crystallography

Diffraction data were collected by the ω-scan technique: for **L** and **C1** at 130(1) K on Rigaku SuperNova four-circle diffractometer with Atlas CCD detector, equipped with Nova microfocus CuK_α radiation source (λ = 1.54178 Å), and for **C2** at 100(1) K, on Rigaku XCalibur four-circle diffractometer with Eos CCD detector, with graphite-monochromatized MoK_α radiation source (λ = 0.71073 Å). The data were corrected for Lorentz-polarization as well as for absorption effects.[55] The structures

This journal is © The Royal Society of Chemistry 2022

Open Access Article. Published on 13 October 2022. Downloaded on 2/5/2023 3:04:53 PM.
This article is licensed under a Creative Commons Attribution 3.0 Unported Licence.

were solved with SHELXT[56] and refined with the full-matrix least-squares procedure on F^2 by SHELXL-2013.[57] All non-hydrogen atoms were refined anisotropically, hydrogen atoms were placed in idealized positions and refined as 'riding model' with isotropic displacement parameters set at 1.2 (1.5 for methyl and hydroxyl groups) times U_{eq} of appropriate carrier atoms. In **C2** the restraints were used for both the geometry and displacement parameters, but no restraints were applied for the cationic parts of the structures. The well-defined, octahedrally symmetrical residual density located across the center of inversion was interpreted as a result of impurity – PF_6 anion. Moreover, the structures of both complexes contained diffused electron density which fills the voids – these effects were taken into account by means of SQUEEZE procedure.[58] In **C1** this unmodeled electron density is probably a result of heavily disordered toluene molecule, in **C2** the best description is a layer of a number of disordered water molecules. The relevant crystallographic data together with the details of structure refinement are listed in Table 2.

NMR titration studies

A solution of ligand of concentration 5×10^{-4} M in CD_3CN was prepared. Then 0.10; 0.25; 0.50; 0.75; 1.00; 1.25 equiv. of Cu $(CH_3CN)_4BF_4$ (stock solution: 5×10^{-3} M in CD_3CN) were added to the solution of ligand and spectra were measured.

UV-Vis titration studies

A solution of **L** at concentration 5.1×10^{-6} M and solutions of $Cu(CH_3CN)_4PF_6$ and $Ni(ClO_4)_2 \cdot 6H_2O$ at concentrations 2×10^{-3} M were prepared in MeCN. 2.5 ml of the ligand solution was poured into a cuvette then the absorption was measured. Next the ligand solution was titrated with Cu(I) [0–1.25 equivalents of Cu^+] or Ni(II) [0–1.65 equivalents of Ni^{2+}] salt.

DNA binding studies

UV-Vis titration. A solution of complex **C1** $[Cu_4L_4]^{4+}$ or **C2** $[Ni_3L_3]^{6+}$ (20 μM) was added to a Tris-HCl buffer solution (pH = 7.22). The prepared samples was titrated with increasing concentration of CT-DNA solution (0–100 μM). A 5-minute time interval was used before each measurement. The binding constant K_b was calculated on the basis of the obtained data using the formula:[59]

$$[DNA]/(\varepsilon_a - \varepsilon_f) = [DNA]/(\varepsilon_b - \varepsilon_f) + 1/K_b\ (\varepsilon_b - \varepsilon_f),$$

where K_b is the intrinsic binding constant, ε_f is coefficient of free compound, ε_a is the extinction coefficient observed (A_{obsd}/[M]), [DNA] is the concentration of CT-DNA in the base pairs and ε_b is the extinction coefficient of the compound fully bound to CT-DNA. In the plot of $[DNA]/(\varepsilon_a - \varepsilon_f)$ *versus* [DNA] K_b value was estimated by the ratio of slope to intercept.

Gibb's standard free energy was calculated from the equation:[60]

$$\Delta G_h^\circ = -RT \ln K_b,$$

where T is temperature, R is gas constant, ΔG_h° is the standard Gibb's free energy, and K_b is the intrinsic binding constant.

Competitive binding with ethidium bromide. A solution consisting of Tris-HCl buffer (pH = 7.22), ethidium bromide (EtBr, 20 μM) and CT-DNA (26 μM) was prepared and incubated in darkness at 24 °C for 30 minutes. Then it was titrated

Table 2 Crystal data, data collection and structure refinement

Compound	L	C1	C2
Formula	$C_{26}H_{24}N$	$(C_{104}H_{96}Cu_4N_{16})^{4+} \cdot 4(PF_6)^- \cdot 6(C_2H_3N) \cdot 2(C_7H_8)$ + disordered solvent	$2(C_{86}H_{88}N_{16}Ni_3O_2)^{6+} \cdot 11(ClO_4)^- \cdot PF_6^- \cdot 2(C_2H_3N) \cdot CH_4O \cdot 4H_2O$ + disordered solvents
Formula weight	392.49	2834.59	4532.73
Crystal system	Monoclinic	Triclinic	Triclinic
Space group	$P2_1/n$	$P\bar{1}$	$P\bar{1}$
a (Å)	6.02703(15)	12.9065(4)	18.3597(7)
b (Å)	13.2413(4)	16.5279(5)	18.4990(7)
c (Å)	12.7941(4)	16.7055(4)	21.3107(8)
α (°)	90	89.181(2)	112.743(4)
β (°)	91.236(2)	76.218(2)	91.517(3)
γ (°)	90	82.422(2)	117.701(4)
V (Å^3)	1020.80(5)	3430.21(17)	5718.5(4)
Z	2	1	1
D_x (g cm^{-3})	1.277	1.372	1.316
F(000)	416	1456	2342
μ (mm^{-1})	0.597	1.893	0.702
Reflections			
Collected	4238	26 696	45 102
Unique (R_{int})	2076 (0.0242)	12 344 (0.0297)	20 107 (0.0428)
With $I > 2\sigma(I)$	1713	10 191	13 671
$R(F)$ [$I > 2\sigma(I)$]	0.0393	0.0554	0.0818
w$R(F^2)$ [$I > 2\sigma(I)$]	0.1002	0.1541	0.2296
$R(F)$ [all data]	0.0504	0.0667	0.1168
w$R(F^2)$ [all data]	0.1121	0.1630	0.2482
Goodness of fit	1.05	1.02	1.10
Max/min $\Delta\rho$ (e Å^{-3})	0.26/−0.17	0.99/−0.39	1.69/−0.81
CCDC number	2097988	2097989	2097990

Open Access Article. Published on 13 October 2022. Downloaded on 2/5/2023 3:04:53 PM.
This article is licensed under a Creative Commons Attribution 3.0 Unported Licence.

with increasing concentration of complex compound $[Cu_4L_4]^{4+}$ or $[Ni_3L_3]^{6+}$ (0–200 μM). The fluorescence spectra were measured in the range of 540–720 nm at λ_{exc} = 467 nm. The solution in the cuvette was incubated for 5 minutes after the addition of each portion of the complex compound solution. Based on the Stern–Volmer equation, the quenching constant was calculated:[61]

$$I_0/I = 1 + K_{SV}[Q],$$

were K_{SV} is the Stern–Volmer constant, I_0 is fluorescence intensities in absence of the quencher, I is fluorescence intensities in presence of the quencher and [Q] is concentration of quencher.

UV melting studies. The spectra were measured at 260 nm in the temperature range 10–95 °C with a temperature increase of 1 °C per minute with nucleic acid concentration of 2.5 μM and **C1** concentration of 10 μM in a sodium cacodyl buffer (pH = 7.5).

GQ induction studies. Tel22 (2 μM) dissolved in Tris-HCl in absence of K^+ (10 mM Tris-HCl, pH = 7.5) was incubated with complexes **C1** and **C2** (0–4 μM). The measurements were performed in the 225–320 nm wavelength range as triplicate.

Protein binding studies

CD analysis of BSA conformational changes. The solutions of BSA (75 nM) in PBS buffer (pH = 7.3) were titrated with the solutions of complexes **C1** (0–37.50 μM) and **C2** $[Ni_3L_3]^{6+}$. The spectra were measured in the range between 204 and 255 nm. MRE (mean of residue ellipticity) was estimated based on:[62]

$$\text{MRE} = [\text{observed CD}/(C_p n l \times 10)], [(\text{deg} \times \text{cm}^2)/\text{dmol}],$$

where l is the optical path cm, C_p is the molar concentration of the protein [mol dm^{-3}] and n = 582 for BSA is number of amino acid residues.

α-Helical content of free and complexed BSA was calculated with the equation:[51]

$$\alpha\text{-Helical } (\%) = [(-\text{MRE}_{209} - 4000)/(33\,000\text{–}4000)] \times 100$$

where 33 000 is the value of the MRE for pure α-helix at 209 nm, while 4000 is the MRE value at 209 nm for random coil conformation and β-form cross.

Fluorescence quenching studies. The BSA solution (5 μM) in PBS buffer (pH = 7.3) was titrated with increasing concentration of complexes. Measurements were made at λ_{exc} = 292 nm in the range 300–550 nm. Based on the modified Stern–Volmer equation, the dynamic quenching constant was calculated:[63]

$$I_0/I = e^{(K_{sv}[Q])}$$

were K_{SV} is the Stern–Volmer constant, I_0 is fluorescence intensities in absence of the quencher, I is fluorescence intensities in presence of the quencher and [Q] is concentration of quencher.

Binding constants and the number of binding sites. Using the Scatchard equation, the static binding constant and the number of binding sites were calculated:[64]

$$\log[(I_0 - I)/I] = \log K_b + n \log[Q]$$

where [Q] is concentration of a quencher, I_0 and I are fluorescence without and with quencher, K_b is the static binding constant of a quencher established from the slope of $\log[(I_0 - I)/I]$ compared with log[Q] and n is number of binding sites.

Author contributions

The manuscript was written through contributions of all authors. All authors have given approval to the final version of the manuscript. Conceptualization, data curation, formal analysis: MSz, MFJ; Funding aquisiton: MSz; Investigation, methodology: MSz, MK, GNR, GC, MFJ; Project administration: MFJ; Resources: MSz; Supervision: MFJ, VP; Validation: MSz, MK, GNR, GC, MFJ; Writing – original draft: MSz, MK, MFJ; Writing – review & editing: MSz, MK, GNR, GC, MFJ, VP.

Conflicts of interest

There are no conflicts to declare.

Acknowledgements

MSz: the work was supported by the National Science Centre, Poland (grant no. 2020/37/N/ST4/00751) and grant no. POWR.03.02.00-00-I026/16 co-financed by the European Union through the European Social Fund under the Operational Program Knowledge Education Development. VP: the work was supported by IDUB-UAM (project no. 006/07/POB3/0006) "International support for AMU staff – international internships as part of the program – International Junior and Senior Exchange".

References

1 M. D. Pluth and K. N. Raymond, *Chem. Soc. Rev.*, 2007, **36**, 161–171.
2 H. Sepehrpour, W. Fu, Y. Sun and P. J. Stang, *J. Am. Chem. Soc.*, 2019, **141**, 14005–14020.
3 Q. Wang, G. Yang, Y. Fu, N. Li, D. Hao and S. Ma, *ChemNanoMat*, 2022, **8**, e202100396.
4 M. Ruben, J. Rojo, F. J. Romero-Salguero, L. H. Uppadine and J.-M. Lehn, *Angew. Chem., Int. Ed.*, 2004, **43**, 3644–3662.
5 H. Zhu, Q. Li, B. Shi, H. Xing, Y. Sun, S. Lu, L. Shangguan, X. Li, F. Huang and P. J. Stang, *J. Am. Chem. Soc.*, 2020, **142**, 17340–17345.

This journal is © The Royal Society of Chemistry 2022

Open Access Article. Published on 13 October 2022. Downloaded on 2/5/2023 3:04:53 PM. This article is licensed under a Creative Commons Attribution 3.0 Unported Licence.

6 R. W. Hogue, S. Dhers, R. M. Hellyer, J. Luo, G. S. Hanan, D. S. Larsen, A. L. Garden and S. Brooker, *Chem. – Eur. J.*, 2017, **23**, 14193–14199.
7 Y. Sun and P. J. Stang, *Aggregate*, 2021, **2**, e94.
8 T. R. Cook and P. J. Stang, *Chem. Rev.*, 2015, **115**, 7001–7045.
9 J.-M. Lehn, *Proc. Natl. Acad. Sci. U. S. A.*, 2002, **99**, 4763–4768.
10 S. H. Hewitt and A. J. Wilson, *Chem. Commun.*, 2016, **52**, 9745–9756.
11 J. W. Steed, D. R. Turner and K. Wallace, *Core Concepts in Supramolecular Chemistry and Nanochemistry*, John Wiley & Sons, West Sussex, U.K., 2007.
12 J. W. Steed and J. L. Atwood, *Supramolecular Chemistry*, John Wiley & Sons, West Sussex, U.K., 2nd edn, 2009.
13 G. Yu, M. Zhang, M. L. Saha, Z. Mao, J. Chen, Y. Yao, Z. Zhou, Y. Liu, C. Gao, F. Huang, X. Chen and P. J. Stang, *J. Am. Chem. Soc.*, 2017, **139**, 15940–15949.
14 M. A. Fik, A. Gorczyński, M. Kubicki, Z. Hnatejko, A. Fedoruk-Wyszomirska, E. Wyszko, M. Giel-Pietraszuk and V. Patroniak, *Eur. J. Med. Chem.*, 2014, **86**, 456–468.
15 A. Adamski, M. A. Fik, M. Kubicki, Z. Hnatejko, D. Gurda, A. Fedoruk-Wyszomirska, E. Wyszko, D. Kruszka, Z. Dutkiewicz and V. Patroniak, *New J. Chem.*, 2016, **40**, 7943–7957.
16 R. Huang and P.-K. Zhou, *Signal Transduction Targeted Ther.*, 2021, **6**, 254.
17 M. A. Muñoz-Lorente, A. C. Cano-Martin and M. A. Blasco, *Nat. Commun.*, 2019, **10**, 4723.
18 M. Marzano, A. P. Falanga, D. Marasco, N. Borbone, S. D'Errico, G. Piccialli, G. N. Roviello and G. Oliviero, *Mar. Drugs*, 2020, **18**, 49.
19 P. L. Scognamiglio, C. Platella, E. Napolitano, D. Musumeci and G. N. Roviello, *Molecules*, 2021, **26**, 3558.
20 C. Vicidomini, F. Cioffi, K. Broersen, V. Roviello, C. Riccardi, D. Montesarchio, D. Capasso, S. Di Gaetano, D. Musumeci and G. N. Roviello, *Future Med. Chem.*, 2019, **11**, 285–302.
21 M. J. Hawkins, P. Soon-Shiong and N. Desai, *Adv. Drug Delivery Rev.*, 2008, **60**, 876–885.
22 A. M. Merlot, D. S. Kalinowski and D. R. Richardson, *Front. Physiol.*, 2014, **5**, 299.
23 B. Deka, T. Sarkar, S. Banerjee, A. Kumar, S. Mukherjee, S. Deka, K. K. Saikia and A. Hussain, *Dalton Trans.*, 2017, **46**, 396–409.
24 T. W. Evans, *Aliment. Pharmacol. Ther.*, 2002, **16**, 6–11.
25 P. Carmeliet and R. K. Jain, *Nature*, 2000, **407**, 249–257.
26 K. Greish, *J. Drug Targeting*, 2007, **15**, 457–464.
27 C. Commisso, S. M. Davidson, R. G. Soydaner-Azeloglu, S. J. Parker, J. J. Kamphorst, S. Hackett, E. Grabocka, M. Nofal, J. A. Drebin, C. B. Thompson, J. D. Rabinowitz, C. M. Metallo, M. G. Vander Heiden and D. Bar-Sagi, *Nature*, 2013, **497**, 633–637.
28 W. Drożdż, A. Walczak, Y. Bessin, V. Gervais, X.-Y. Cao, J.-M. Lehn, S. Ulrich and A. R. Stefankiewicz, *Chem. – Eur. J.*, 2018, **24**, 10802–10811.
29 W. Drożdż, Y. Bessin, V. Gervais, X.-Y. Cao, J.-M. Lehn, A. R. Stefankiewicz and S. Ulrich, *Chem. – Eur. J.*, 2018, **24**, 1518–1521.
30 O. Domarco, D. Lötsch, J. Schreiber, C. Dinhof, S. Van Schoonhoven, M. D. García, C. Peinador, B. K. Keppler, W. Berger and A. Terenzi, *Dalton Trans.*, 2017, **46**, 329–332.
31 A. T. Phan, V. Kuryavyi, S. Burge, S. Neidle and D. J. Patel, *J. Am. Chem. Soc.*, 2007, **129**, 4386–4392.
32 Y. Zhang, X. Yan, L. Shi, M. Cen, J. Wang, Y. Ding and Y. Yao, *Inorg. Chem.*, 2021, **60**, 7627–7631.
33 W. Drożdż, C. Bouillon, C. Kotras, S. Richeter, M. Barboiu, S. Clément, A. R. Stefankiewicz and S. Ulrich, *Chem. – Eur. J.*, 2017, **23**, 18010–18018.
34 A. R. Stefankiewicz, J. Harrowfield, A. M. Madalan and J.-M. Lehn, *CrystEngComm*, 2013, **15**, 9128–9134.
35 A. Gorczyński, M. Kubicki, K. Szymkowiak, T. Łuczak and V. Patroniak, *RSC Adv.*, 2016, **6**, 101888–101899.
36 S. Napierała, M. Kubicki, V. Patroniak and M. Wałęsa-Chorab, *Electrochim. Acta*, 2021, **369**, 137656.
37 B. Schäfer, J.-F. Greisch, I. Faus, T. Bodenstein, I. Šalitroš, O. Fuhr, K. Fink, V. Schünemann, M. M. Kappes and M. Ruben, *Angew. Chem., Int. Ed.*, 2016, **55**, 10881–10885.
38 V. Patroniak, J.-M. Lehn, M. Kubicki, A. Ciesielski and M. Wałęsa, *Polyhedron*, 2006, **25**, 2643–2649.
39 V. Patroniak, P. Baxter, J.-M. Lehn, M. Kubicki, M. Nissinen and K. Rissanen, *Eur. J. Inorg. Chem.*, 2003, **2003**, 4001–4009.
40 N. Suryadevara, A. Pausch, E. Moreno-Pineda, A. Mizuno, J. Bürck, A. Baksi, T. Hochdörffer, I. Šalitroš, A. S. Ulrich, M. M. Kappes, V. Schünemann, W. Klopper and M. Ruben, *Chem. – Eur. J.*, 2021, **27**, 15172–15180.
41 H. Han and L. H. Hurley, *Trends Pharmacol. Sci.*, 2000, **21**, 136–142.
42 S. Mulliri, A. Laaksonen, P. Spanu, R. Farris, M. Farci, F. Mingoia, G. N. Roviello and F. Mocci, *Int. J. Mol. Sci.*, 2021, **22**, 6028.
43 B. J. Pages, D. L. Ang, E. P. Wright and J. R. Aldrich-Wright, *Dalton Trans.*, 2015, **44**, 3505–3526.
44 N. J. Wheate, C. R. Brodie, J. G. Collins, S. Kemp and J. R. Aldrich-Wright, *Mini-Rev. Med. Chem.*, 2007, **7**, 627–648.
45 J. Portugal, D. J. Cashman, J. O. Trent, N. Ferrer-Miralles, T. Przewloka, I. Fokt, W. Priebe and J. B. Chaires, *J. Med. Chem.*, 2005, **48**, 8209–8219.
46 G. Zhou, X. Liu, Y. Li, S. Xu, C. Ma, X. Wu, Y. Cheng, Z. Yu, G. Zhao and Y. Chen, *Oncotarget*, 2016, **7**, 14925–14939.
47 F. Greco, D. Musumeci, N. Borbone, A. P. Falanga, S. D'Errico, M. Terracciano, I. Piccialli, G. N. Roviello and G. Oliviero, *Molecules*, 2022, **27**, 2997.
48 M. A. Fik-Jaskółka, I. Pospieszna-Markiewicz, G. N. Roviello, M. Kubicki, W. Radecka-Paryzek and V. Patroniak, *Inorg. Chem.*, 2021, **60**, 2122–2126.
49 X. M. He and D. C. Carter, *Nature*, 1992, **358**, 209–215.
50 M. A. Fik-Jaskółka, A. F. Mkrtchyan, A. S. Saghyan, R. Palumbo, A. Belter, L. A. Hayriyan, H. Simonyan,

Open Access Article. Published on 13 October 2022. Downloaded on 2/5/2023 3:04:53 PM.
This article is licensed under a Creative Commons Attribution 3.0 Unported Licence.

V. Roviello and G. N. Roviello, *Spectrochim. Acta, Part A*, 2020, **229**, 117884.
51 M. A. Fik-Jaskółka, A. F. Mkrtchyan, A. S. Saghyan, R. Palumbo, A. Belter, L. A. Hayriyan, H. Simonyan, V. Roviello and G. N. Roviello, *Amino Acids*, 2020, **52**, 755–769.
52 N. Raman, K. Pothiraj and T. Baskaran, *J. Mol. Struct.*, 2011, **1000**, 135–144.
53 J. Marmur, *J. Mol. Biol.*, 1961, **3**, 208–218.
54 M. E. Reichmann, S. A. Rice, C. A. Thomas and P. Doty, *J. Am. Chem. Soc.*, 1954, **76**, 3047–3053.
55 A. Technologies, *CrysAlis PRO (Version 1.171.39.46)*, Agilent Technologies Ltd, 2018.
56 G. Sheldrick, *Acta Crystallogr., Sect. A: Found. Adv.*, 2015, **71**, 3–8.
57 G. Sheldrick, *Acta Crystallogr., Sect. C: Struct. Chem.*, 2015, **71**, 3–8.
58 A. Spek, *Acta Crystallogr., Sect. C: Struct. Chem.*, 2015, **71**, 9–18.
59 L. Shivakumar, K. Shivaprasad and H. D. Revanasiddappa, *Spectrochim. Acta, Part A*, 2012, **97**, 659–666.
60 D. Sabolová, M. Kožurková, T. Plichta, Z. Ondrušová, D. Hudecová, M. Šimkovič, H. Paulíková and A. Valent, *Int. J. Biol. Macromol.*, 2011, **48**, 319–325.
61 B. C. Baguley and M. Le Bret, *Biochemistry*, 1984, **23**, 937–943.
62 F. Shiri, M. Rahimi-Nasrabadi, F. Ahmadi and H. Ehrlich, *Spectrochim. Acta, Part A*, 2018, **203**, 510–521.
63 V. M. Manikandamathavan, M. Thangaraj, T. Weyhermuller, R. P. Parameswari, V. Punitha, N. N. Murthy and B. U. Nair, *Eur. J. Med. Chem.*, 2017, **135**, 434–446.
64 X.-Z. Feng, Z. Lin, L.-J. Yang, C. Wang and C. I. Bai, *Talanta*, 1998, **47**, 1223–1229.

This journal is © The Royal Society of Chemistry 2022